ACS APPLIED MATERIALS & INTERFACES

Research Article

www.acsami.org

Enhanced Electrochemical Performance of ZnO-Loaded/Porous Carbon Composite as Anode Materials for Lithium Ion Batteries

Xueyang Shen, Daobin Mu,* Shi Chen, Borong Wu, and Feng Wu

Beijing Key Laboratory of Environmental Science and Engineering, School of Chemical Engineering and Environment, Beijing Institute of Technology, Beijing 100081, China

ABSTRACT: ZnO-loaded/porous carbon (PC) composites with different ZnO loading amounts are first synthesized via a facile solvothermal method and evaluated for anode materials of lithium ion batteries. The architecture and the electrochemical performance of the as-prepared composites are investigated through structure characterization and galvanostatic charge/discharge test. The ZnO-loaded/PC composites possess a rich porous structure with well-distributed ZnO particles (size range: 30−100 nm) in the PC host. The one with 54 wt % ZnO loading contents exhibits a high reversible capacity of 653.7 mA h g^{-1} after 100 cycles. In particular, a capacity of 496.8 mA h g^{-1} can be reversibly obtained when cycled at 1000 mA g^{-1}. The superior lithium storage properties of the composite may be attributed to its nanoporous structure together with an interconnected network. The modified interfacial reaction kinetics of the composite promotes the intercalation/deintercalation of lithium ions and the charge transfer on the electrode. As a result, the enhanced capacity of the composite electrode is achieved, as well as its high rate capability.

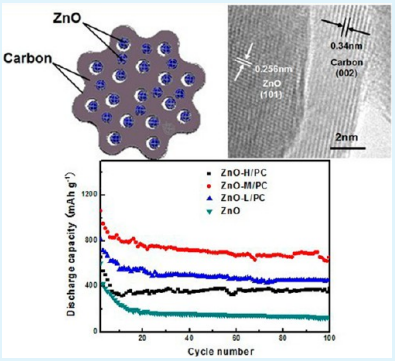

KEYWORDS: *zinc oxide, porous carbon, composite, anode material, lithium ion batteries*

1. INTRODUCTION

Long-lasting and green rechargeable energies are in high demand to solve the dilemma of global environmental pollution and energy shortage.[1] Among various renewable batteries, lithium ion batteries (LIBs) have attracted increasing attention for their applications in portable electronics and electric vehicles in recent years.[2,3] For the requirement of high-performance LIBs, novel anode materials have become one of the research hotspots nowadays. Zinc oxide (ZnO) is such a potential candidate because of its attractive theoretical capacity of 978 mA h g^{-1}.[4] As a well-known functional material, it has been widely applied in various fields of solar cells, optoelectronic devices, gas sensors, and Zn/Ni secondary batteries.[5−8] However, it is seldom used as a LIB anode material, since some drawbacks have not been overcome yet. The inferior cyclability is such a critical problem limiting its application that the capacity fades severely even at low current densities.[9−11] Some studies are involved with the cycle performance modification of ZnO anode, including the fabrication of nanostructured materials such as nanorods and nanowires;[10,11] the modification by TiO_2, Ni, and carbon coating on the electrode;[12−14] and the preparation of ZnO-based composites.[15−17] Nonetheless, the anode usually delivers a reversible capacity below 500 mA h g^{-1}, which is far less than its theoretical value, and its high rate capability is not satisfied either.[10−17] There is still much room for the performance improvement of ZnO-based anode.

To enable high reversible capacity, ZnO anode materials should possess good electronic conductibility and structural stability. In addition, the solid-state diffusion of lithium ion is usually considered to be a rate-limited step, which could be enhanced by increasing the porosity of electrodes.[18] Huang and co-workers prepared porous ZnO nanosheets through a chemical bath deposition.[19] The anode material exhibited a capacity of 400 mA h g^{-1} after 100 cycles at a current density of 500 mA g^{-1}. It may be the porous nanostructure that plays an important role in the improved rate performance, although the specific capacity is still far from the theoretical capacity of ZnO. Recently, porous carbon (PC) has been used as a dispersing medium for metal oxides (TiO_2, SnO_2, Fe_3O_4, etc.),[20−22] because of its advantages like excellent conductive network and good strain accommodation. In these studies, PC is capable of benefiting the stress relaxation, and then preventing the metal oxide electrodes from aggregation and pulverization. However, no such modification has been found on ZnO anode so far.

In our report, we first attempt to synthesize ZnO-loaded/PC composite through a facile solvothermal approach using PC as a host medium. In the synthesis, ZnO crystals could be well-distributed in the PC host under high pressure during the boiling process. Besides, as a result of the pore-directed effect, the porous structured carbon plays a decisive role in controlling the size and shape of the loading ZnO particles. The effect of the porosity on lithium storage properties of the as-prepared composites is discussed. The structure, morphology, and electrochemical performance of the ZnO-loaded/PC composites with different ZnO contents are investigated in detail.

Received: January 3, 2013
Accepted: March 26, 2013
Published: March 26, 2013

 © 2013 American Chemical Society

2. EXPERIMENTAL SECTION

Composites Preparation. Porous carbon was prepared by a template method based on our previous work.[23] Gelatin (Beijing Chemical Works, 99%, AR) and nano-$CaCO_3$ (Shanghai Aladdin, GR) particulates (in size around 30−50 nm) were used as a carbon source and template, respectively (gelatin:$CaCO_3$ = 2:1, wt %). The calcination treatment was conducted at 700 °C for 2 h under an argon atmosphere.

A solvothermal method was used to synthesize the ZnO-loaded/PC composites. The illustration of the synthesis is in Figure 1. A short-chain polymer (PEG 400, Beijing Chemical Works) was employed as a dispersant to avoid the agglomeration of the growing ZnO particles. First, $Zn(CH_3COO)_2{\cdot}2H_2O$ (2 g, Beijing Chemical Works, 99%, AR) was dissolved in a mixture of 14 mL of polyethylene glycol (PEG 400) and 76 mL of ethanol solution. Then, a certain amount (0.25, 0.5, and 1 g) of PC was added into the solution, respectively, under magnetic stirring for 15 min. Correspondingly, ZnO-H/PC, ZnO-M/PC, and ZnO-L/PC were used to represent the three samples. Next, the above mixture was transferred into a 100 mL Teflon-lined autoclave, followed by the addition of 0.7 g of solid NaOH (Beijing Chemical Works, 96%, AR). The autoclave was sealed and maintained at 140 °C for 24 h and then cooled down to room temperature naturally. The precipitates were filtered off, washed with deionized water, and vacuum-dried at 50 °C for 10 h. Similarly, pure ZnO was also prepared through the above process without the addition of PC.

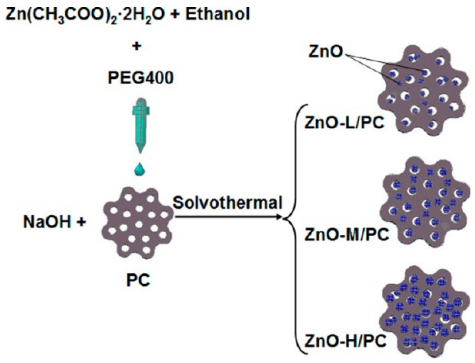

Figure 1. The illustration of the synthesis of the ZnO-loaded/PC composites.

Composites Characterization. X-ray diffraction (XRD) patterns of the samples were obtained using an Ultima IV diffractometer (UltimaIV-185, Rigaku) with filtered Cu Ka radiation (scan rate: 8° min^{-1}, 10−80°). Scanning electron microscopy measurements were conducted on a JEOL JSM-5600LV instrument operated at 15 kV. Transmission electron microscope (TEM) images were taken using a JEM-2100F electron microscope with an acceleration voltage of 200 kV. Nitrogen sorption isotherms were measured on a NOVA1200 instrument (Quantachrome Corporation) at 77 K. Prior to the measurement, the samples were degassed in a vacuum at 200 °C for 12 h. The Brunauer−Emmett−Teller (BET) method was utilized to calculate the specific surface area. The pore size distribution was derived from the desorption branches of the isotherms using the Barrett−Joyner−Halenda (BJH) method. The total pore volume was estimated at a relative pressure of 0.98. The loading amounts of ZnO in the composites were examined by thermogravimetry (TG) analysis using a SEIKO TG/DTA6300 instrument at a ramping rate of 10 °C min^{-1} in air. The temperature range was 30−800 °C.

Electrochemical Test. Electrochemical measurements were performed using coin-type cells (CR 2025) with lithium metal as the counter and reference electrodes at room temperature. The working electrode was prepared by coating the slurry of active material, carbon black, and polyvinylidene fluoride (6:2:2 in weight ratio) dissolved in methyl pyrrolidinone onto a Cu foil substrate, and dried at 100 °C for 10 h before testing. Cell assembly was carried out in an argon-filled glovebox (the concentrations of moisture and oxygen below 1 ppm). The electrolyte (Guotai Huarong New Chemical Materials Co., Ltd.) was 1 mol L^{-1} $LiPF_6$/EC + DEC solution (EC:DEC = 1:1 in weight ratio), and the separator in the coin cell was Celgard 2300 film. The cells were charged/discharged by galvanostatic cycling between 0.01 and 3 V at various current densities (100, 200, 500, and 1000 mA g^{-1}) using a LAND 2001 CT battery tester. Cyclic voltammetry (CV) of the electrode was measured at a scan rate of 0.1 mV s^{-1}. Electrochemical impedance spectroscopy (EIS) measurements were performed on an electrochemical workstation (CHI 660 D, CHI Company) under a frequency range between 100 kHz and 0.1 Hz with an applied voltage of 10 mV. The voltages mentioned in this study were referred to a Li/Li^+ redox couple.

3. RESULTS AND DISCUSSION

The XRD patterns of the samples with various loading levels of ZnO are shown in Figure 2. For comparison, the spectra of the as-prepared pure ZnO and PC are also given. The broad peak around 23° in the XRD pattern of PC corresponds to the (002) plane of the carbon phase with non-graphitized structure.[24] After the loading of ZnO, the diffraction peaks appearing at 2θ = 31.6, 34.4, 36.2, 47.5, 56.5, 62.9, 66.3, 67.8, 69° can be indexed as the wurtzite phase of ZnO with the planes of (100), (002), (101), (102), (110), (103), (200), (112), and (201), respectively (PDF No. 36-1541). The intensities of the ZnO characteristic peaks increase along with the increasing loading level of ZnO, while the intensity of the broad carbon peak

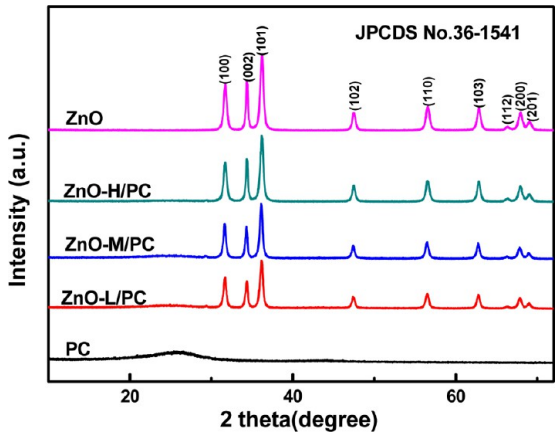

Figure 2. XRD patterns of ZnO nanorods, PC, and ZnO-loaded/PC composites with different ZnO contents.

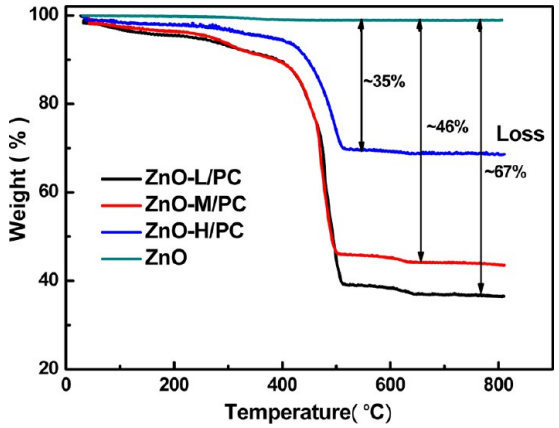

Figure 3. TG curves of ZnO-loaded/PC composites under air atmosphere from 30 to 800 °C.

dx.doi.org/10.1021/am400020n | ACS Appl. Mater. Interfaces 2013, 5, 3118−3125

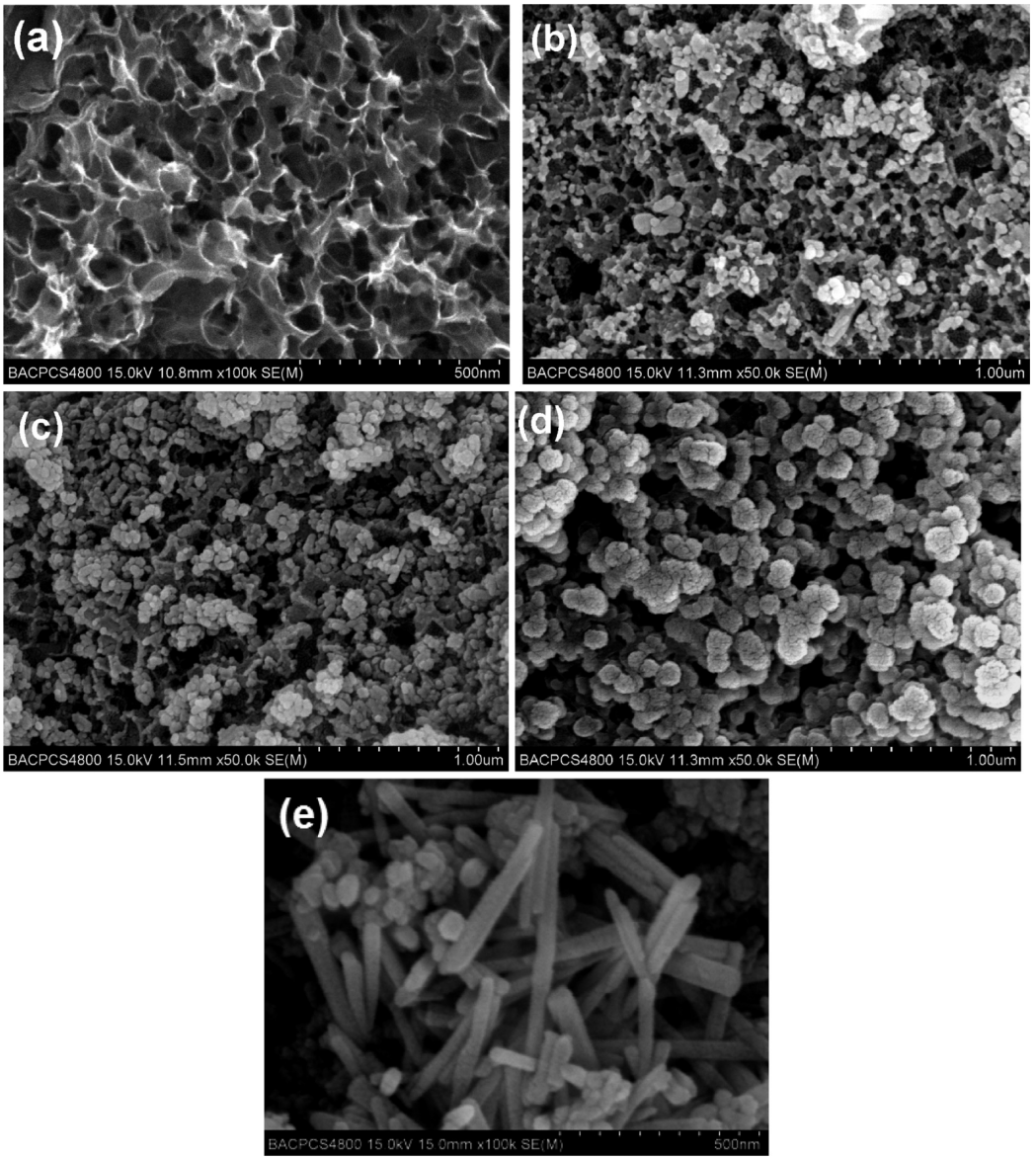

Figure 4. SEM images of (a) PC, (b) ZnO-L/PC, (c) ZnO-M/PC, (d) ZnO-H/PC composites, and (e) ZnO nanorods,.

decreases. Therefore, the as-prepared sample is primarily composed of ZnO and carbon phases.

The content of ZnO in the composite was estimated by thermogravimetric (TG) analysis, with the results shown in Figure 3. Over the temperature range from 400 to 500 °C, there is an obvious weight loss for all three samples, which can be ascribed to the combustion of PC in air. Almost no weight loss is accompanied as the temperature increases. Therefore, the total mass loss is around 35, 46, and 67% for the three samples. Correspondingly, the amount of ZnO is estimated to be 65 wt % (ZnO-H/PC), 54 wt % (ZnO-M/PC), and 33 wt % (ZnO-L/PC).

The SEM morphology of the PC is shown in Figure 4a, displaying a highly developed porous fabrication. The pores are well-distributed with a size of 30−50 nm, which is larger than that of conventional mesoporous carbon CMK-3 (2−10 nm). Thus, it may provide enough space to accommodate the subsequent loading of ZnO crystals. Figure 4b−d gives the SEM images of ZnO-loaded/PC composites with different ZnO loading contents. It is seen that the ZnO particles are well dispersed in the pores and the surface of the PC host. With increasing ZnO contents, the particle size of the loaded ZnO gets bigger. When the loading level is controlled to be 65%, the average diameter of ZnO is near 100 nm, which is larger than both cases of 54% (50 nm) and 33% (30 nm). The higher loading level also raises the chance for the particle aggregation of ZnO. Upon the case without adding PC during synthesis, ZnO nanorods are generated in a size range from 30 to 50 nm, as shown in Figure 4e. The transformation of the morphology from pure ZnO nanorods to nanoparticles in the composites may be ascribed to the pore-directed effect of PC. Furthermore, the short-chain polymer PEG400 may selectively promote the anisotropic growth of ZnO in the synthesis process, thus ensuring the good distribution of ZnO in the PC host. PC acts as not only a host material but also the source of pores for the composites.

Figure 5a shows the nitrogen adsorption−desorption isotherms of ZnO nanorods and ZnO-loaded/PC composites. The corresponding data are listed in Table 1. ZnO nanorods exhibit fairly low porosity with a specific surface area of 25.4 m^2

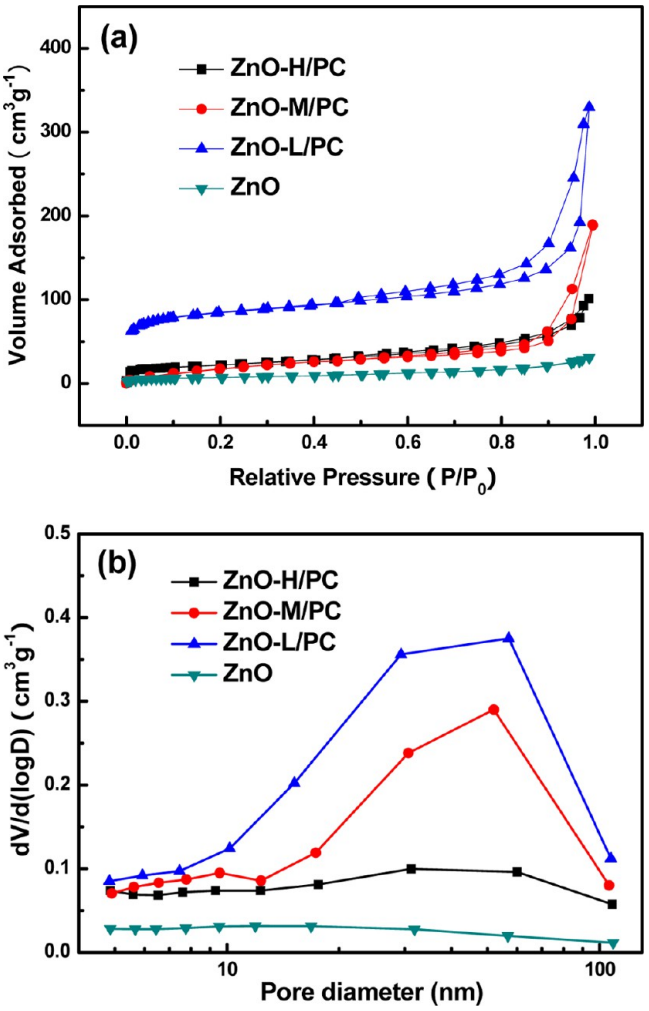

Figure 5. (a) N_2 adsorption/desorption isotherms of ZnO and ZnO-loaded/PC composites. (b) Pore size distributions of ZnO and ZnO-loaded/PC composites (the samples were degassed under a vacuum at 200 °C for 12 h before the measurements).

Table 1. Textural Properties of ZnO Nanorods and ZnO-Loaded/PC Composites with Different ZnO Contents

sample	BET surface area (m^2 g^{-1})	pore volume (cm^3 g^{-1})
ZnO	25.4	0.04
ZnO-H/PC	77.52	0.16
ZnO-M/PC	234.6	0.29
ZnO-L/PC	319.11	0.43

g^{-1} and a pore volume of 0.04 m^3 g^{-1}. As for the ZnO-loaded/PC composites, high porosity is achieved due to the introducing host with developed porous structure. The specific surface area and the pore volume of ZnO-H/PC are 319.11 m^2 g^{-1} and 0.43 m^3 g^{-1}, respectively, which are 10 times more than those of pure ZnO nanorods. In the isotherms of the composite, a typical H1 hysteresis loop in mesopore range confirms its porosity further. The specific surface area and the pore volume of the three composites both decrease gradually accompanied with the increasing content of ZnO. It is implied that ZnO is successfully loaded in the PC host. Figure 5b illustrates the pore diameter distribution of the above samples according to BJH calculation. In the case of the composites, the pore size distributes in the mesopore range 30−50 nm, while

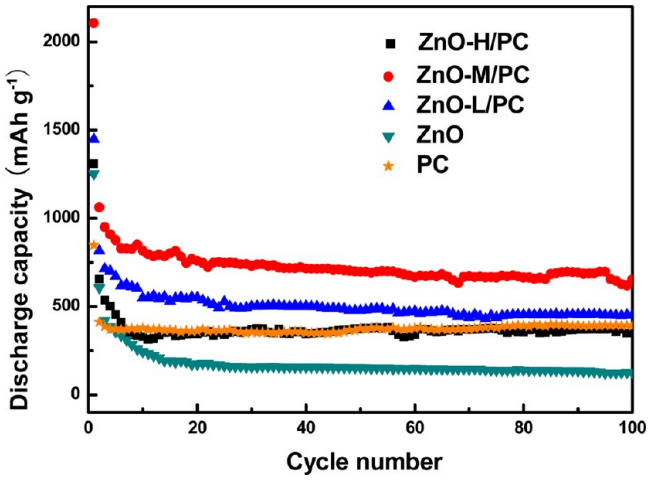

Figure 6. Cycling performance of ZnO nanorods and ZnO-loaded/PC composites with different ZnO contents at a current density of 100 mA g^{-1}.

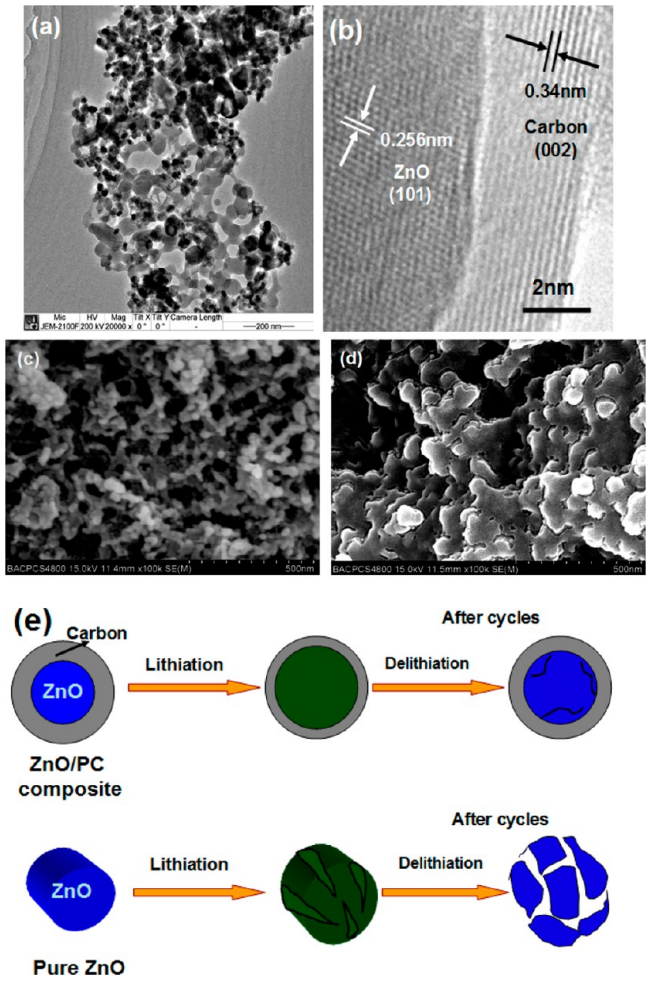

Figure 7. (a) TEM and (b) HRTEM images of ZnO-M/PC composite; SEM images of (c) ZnO-M/PC composite and (d) ZnO electrode after charge/discharge cycles; (e) schematic illustration of volume change during lithiation/delithiation processes.

no pore diameter can be detected for ZnO nanorods. Moreover, the declined $dV/d(\log D)$ of the composite provides more proof for ZnO occupation in the pores of PC.

dx.doi.org/10.1021/am400020n | ACS Appl. Mater. Interfaces 2013, 5, 3118−3125

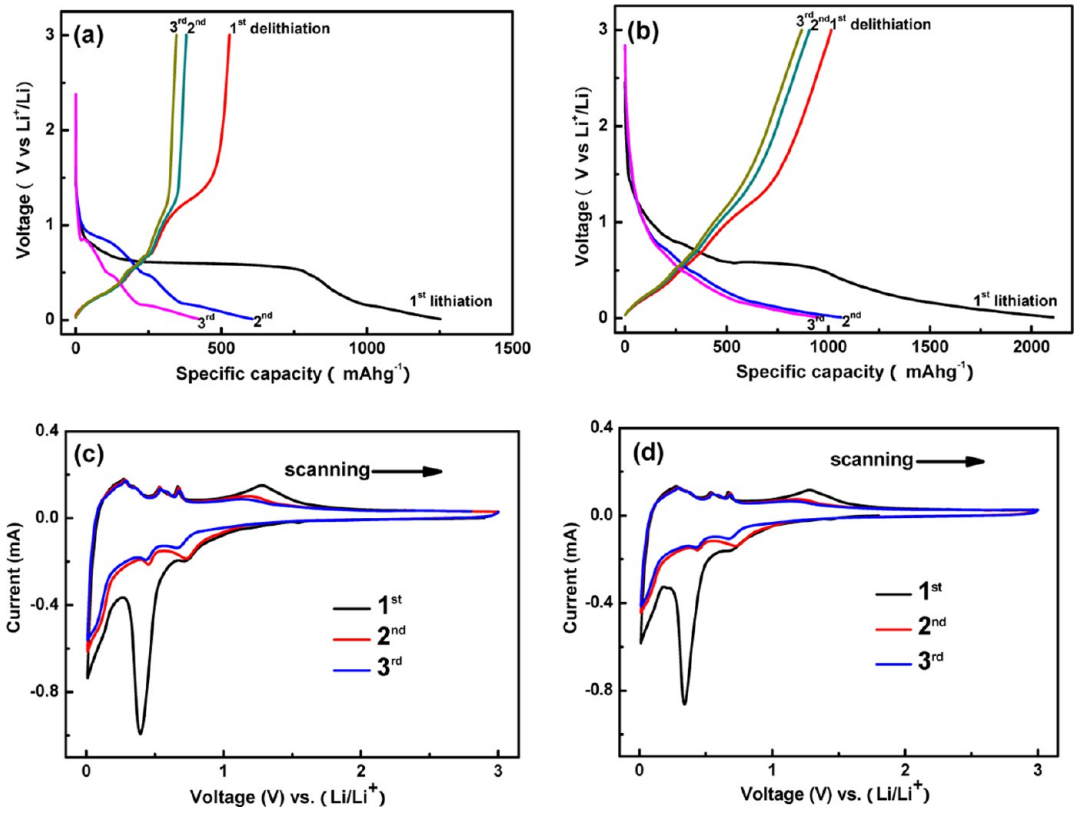

Figure 8. Charge–discharge curves of (a) ZnO and (b) ZnO-M/PC composite electrode cycled between 0 and 3 V at a current density of 100 mA g^{-1}. Cyclic voltammogram curves of (c) ZnO and (d) ZnO-M/PC composite electrode in the initial three cycles. The scan rate is 0.1 mV s^{-1}.

Figure 6 shows the cycling performance of ZnO nanorods and ZnO-loaded/PC composite electrodes. The ZnO-M/PC electrode exhibits the highest discharge capacity of 653.7 mA h g^{-1} after 100 cycles among the four samples. It is much higher than the values of ZnO-L/PC (450.2 mA h g^{-1}) and ZnO-H/PC (375.7 mA h g^{-1}) electrodes. The pure ZnO electrode keeps a low reversible capacity of 123.3 mA h g^{-1} under the same conditions, which is only about 9.8% of the initial discharge capacity. The reason for the improved cycling performance of the ZnO-loaded/PC composites can be ascribed to the advantages of the porous structure with embedded ZnO nanoparticles, while an appropriate porosity is a key factor in discussing the reversible capacities of various ZnO-loaded/PC composites. As for the ZnO-L/PC, the low loading level of ZnO leads to the unsatisfied discharge capacity. In the meanwhile, overly developed porosity increases the chance to intercalate irreversibly lithium ion. In the case of ZnO-H/PC, excessive ZnO particles may block the pores of the PC host, which is unfavorable for keeping the porous structure of the composite. Besides, the high loading level of ZnO (64 wt %) results in larger ZnO particles, as observed in SEM images, together with an increase in the mechanical stress of the composite. Thus, it can be concluded that the optimal cycling performance of ZnO-M/PC benefits from the appropriate porosity in the composite, as well as the loading amount of ZnO.

The TEM image of ZnO-M/PC shown in Figure 7a further manifests the uniform distribution of ZnO in the PC host without apparent aggregation. The HRTEM image (Figure 7b) gives the morphology of the ZnO embedment structure. The lattice spacing accords well with the interplanar spacing (0.256 nm) of the (101) plane of ZnO crystal,[25] while the surrounding phase shows a lattice spacing of 0.34 nm, corresponding to the *d* spacing of the (002) plane of carbon structure.[26] The result strongly confirms the embedment of ZnO in PC host. Additionally, the morphology change of ZnO-M/PC composite and ZnO nanorod electrodes after being charged/discharged is shown in Figure 7c and d. It is clear that the morphology of ZnO electrode (Figure 7d) after cycling had drastically changed compared with that of the fresh electrode (Figure 4e). This indicates that the active material ZnO deteriorates severely with the lithiation/delithiation process, leading to the apparent decline of the reversible capacity. On the contrary, as shown in Figure 7c, the ZnO-M/PC electrode almost keeps the original morphology with no obvious pulverization or cracks after cycles. Moreover, the porous structure of the composite electrode still remains. This process can be visually described in Figure 7e. It suggests that a PC host with porous network provides accommodation room for the huge volume change of the ZnO particles during Li ion intercalation and deintercalation, and alleviates the degradation of the electrode with cycling. This nanoporous structure thus can sustain the good cycle stability of the composite electrode.

The discharge–charge voltage profiles of the ZnO-M/PC composite and pure ZnO electrodes are shown in Figure 8a and b. The composite electrode delivers initial discharge/charge capacities of 2107.4 and 1062.9 mA h g^{-1}, respectively, which is much higher than the values of pure ZnO (1251.8 and 606.4 mA h g^{-1}). Such increased lithium storage capacity may be due to the modified nanoporous structure by introducing the PC host. In addition, the active ZnO particles can be more sufficiently utilized with its dispersion in the pores of PC. There exists a long voltage plateau near 0.5 V for both electrodes in the first discharge cycle, but it disappears in the subsequent

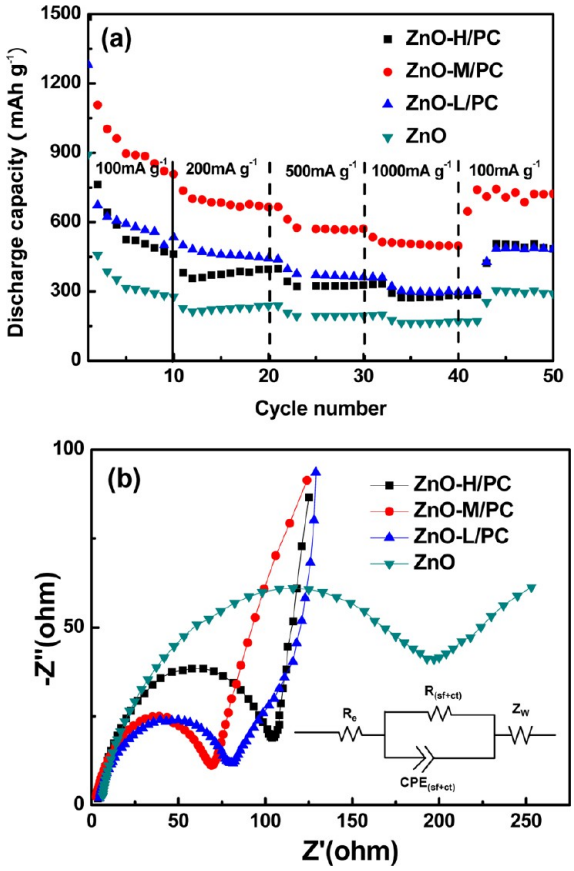

Figure 9. (a) Rate performance and Coulombic efficiency of ZnO-loaded/PC composites with different ZnO contents and pure ZnO electrodes cycled between 0.1 and 3 V. (b) Nyquist plots at the OCP (10 mV perturbation) and the equivalent circuit for the electrodes.

Table 2. Kinetic Parameters of ZnO Nanorods and ZnO-Loaded/PC Composites Based on Modeling AC Impendence Spectra

electrode	R_e (Ω)	$R_{(sf+ct)}$ (Ω)	i_0, (A cm^{-2})	D_{Li^+} (cm^2 S^{-1})
ZnO-H/PC	2.393	113.1	1.15×10^{-4}	1.11×10^{-8}
ZnO-M/PC	1.199	73.99	1.77×10^{-4}	1.4×10^{-8}
ZnO-L/PC	2.224	85.78	1.52×10^{-4}	1.67×10^{-8}
ZnO	2.787	215.2	6.07×10^{-5}	1.34×10^{-16}

cycles. This phenomenon reflects the initial irreversible capacity loss which is mainly due to the formation of SEI film. The plateau at about 0.8 V from the second scan is caused by the lithiation of ZnO. Unlike the pure ZnO, a plateau near 0.1 V can be seen in the discharge curves of the composite electrode, which may be ascribed to the lithiation contribution of PC.

In Figure 8c and d, cyclic voltammograms of the ZnO-M/PC composite and pure ZnO electrodes were obtained at a scan rate of 0.1 mV s^{-1}. In the first cathodic half-cycle (lithiation), a strong reduction peak nearby 0.35 V can be observed in both of the pure ZnO and composite electrodes. It should be assigned to the two-step reaction of ZnO with lithium and the formation of the solid electrolyte interphase (SEI) layer.[12] According to the reports,[4,19] the electrochemical process of ZnO with lithium consists of the reduction of ZnO into Zn and the formation of lithium−zinc alloy, which can be written as follows.

$$ZnO + 2Li \rightarrow Zn + Li_2O \quad (1)$$

$$Zn + Li \rightarrow LiZn \quad (2)$$

The voltages of these reactions are so close that they only correspond to a strong peak. After the first cycle, the reduction peaks at around 0.4 and 0.7 V without apparent shift, indicating that the lithiation process of ZnO keeps reversibly. In the first anodic half-cycle (delithiation), the oxidation peaks appearing at potentials below 1.0 V (0.3, 0.53, and 0.68 V) can be ascribed to the multistep delithiation process of lithium−zinc alloy.[9] The peak at 1.3 V should be related to the formation of ZnO with the reaction between Zn and Li_2O.[27] However, the reaction becomes weak from the second scan and hardly proceeds with cycling. This may be due to the incomplete conversion of Zn to ZnO.

The ZnO-loaded/PC composite electrodes also display enhanced rate performance, as shown in Figure 9a. It is found that the ZnO-M/PC composite has the optimal high rate capability among the tested electrodes. The reversible capacities of the ZnO-M/PC composite are 665.1 and 512.7 mA h g^{-1} at the current densities of 200 and 500 mA g^{-1}, respectively. A value of 496.8 mA h g^{-1} can still be retained even at 1000 mA g^{-1}. When the charge/discharge system is back to the low current rate of 100 mA g^{-1}, the discharge capacities can recover to the same level. The electrode exhibits a superior rate performance in comparison with presently reported results,[4,11,12,17,28] as shown in Table 3. Electrochemical impedance spectra (EIS) of the electrodes are shown in Figure 9b. The intercept at the real impedance axis in the high-frequency region corresponds to the ohmic resistance (R_e). It represents the total resistance of the electrolyte and electrical contacts. The semicircle in the high frequency region can be

Table 3. Comparison of Cycling and Rate Performance among ZnO-Based Anodes

sample	reversible capacity (mA h g^{-1})	cycle number	voltage (V)	rate	ref
ZnO arrays	237.7	50th	0−3	0.5C	17
	157.2	50th	0−3	2C	
ZnO-C arrays	315.7	50th	0−3	0.5C	
	127.6	50th	0−3	2C	
ZnO nanowire	252	30th	0.005−2	120 mA g^{-1}	11
ZnO microrod	500	100th	0−3	50 mA g^{-1}	4
flower-like ZnO	480	50th	0.02−3	500 mA g^{-1}	28
	392	50th	0.02−3	120 mA g^{-1}	
ZnO nanorod	358	30th	0.3−3	50 mA g^{-1}	12
TiO_2-coated ZnO	447	30th	0.3−3	50 mA g^{-1}	
ZnO-U/PC	653.7	100th	0.1−3	100 mA g^{-1}	this work
composite	512.7	10th	0.1−3	500 mA g^{-1}	

dx.doi.org/10.1021/am400020n | ACS Appl. Mater. Interfaces 2013, 5, 3118−3125

assigned to the charge-transfer resistance (R_{ct}) and the SEI film resistance (R_{sf}).[29,30] The straight line in the low frequency region is associated with the lithium diffusion process within electrodes. The kinetic data of ZnO nanorods and ZnO-loaded/PC composites are shown in Table 2. No distinct difference exists in the R_e values of four samples, indicating that the cells have the same test conditions. The resistance sums (R_{sf+ct}) of the ZnO-loaded/PC composite electrodes are smaller than that of the pure ZnO electrode, indicating the higher electrochemical activity and better utilization of the electrodes. In terms of the following equations:[31−34]

$$i_0 = \frac{RT}{nFR_{ct}} \tag{3}$$

$$D_{Li^+} = \frac{R^2T^2}{2A^2F^4C^2n^4\sigma^2} \tag{4}$$

where R is the gas constant, T is the absolute temperature, n is the number of transferred electrons, F is the Faraday constant, A is the surface area of the electrode, C is the concentration of Li^+ in the electrode, and σ is Warburg factor obeying the relationship:

$$Z_{re} = \sigma\cdot\omega^{-1/2} \tag{5}$$

The exchange current densities i_0 and lithium diffusion coefficient D_{Li^+} of the ZnO-L/PC, ZnO-M/PC, and ZnO-H/PC electrodes are calculated, as shown in Table 2. The values of i_0 and D_{Li^+} of the ZnO-loaded/PC composite electrodes are much higher than those of the ZnO nanorod electrode. It further demonstrates the good lithium intercalation kinetics in the composite electrodes. Moreover, the Nyquist impedance plot of the composites exhibits a line with a slope close to 90° in the low frequency region, indicating a characteristic of capacitive property.[35,36] Thus, it is reasonable to exhibit the high rate performance in the composite electrodes. The modified interfacial reaction kinetics can be supposed to the consequence of the rich porosity and good electric contact of the composite. The porous structure is beneficial to increasing the contact area between the electrode and the electrolyte, thereby increasing the reaction area and active sites. Additionally, as a result of the enhanced conductive network, the strong electronic interconnection of the active materials guarantees the faster charge transfer on the electrode. These make a great contribution to the improved rate capability of ZnO-loaded/PC composites.

4. CONCLUSIONS

In conclusion, ZnO-loaded/PC composites are first synthesized as anode materials for LIBs via a facile solvothermal method. This in situ process leads to good distribution of ZnO particles in the PC host. Electrochemical test results show that all of the as-prepared ZnO-loaded/PC composites exhibit superior cycle stability and rate capability compared to those of pure ZnO. Especially when the loading level of ZnO is controlled to be 54 wt %, the composite electrode displays an outstanding reversible capacity of 653.7 mA h g^{-1} after 100 cycles as well as a high rate capacity of 496.8 mA h g^{-1} at 1000 mA g^{-1}. The carbon host with porous network can provide accommodation room for the volume change of the ZnO particles during cycling, thus alleviating the degradation of the composite electrode and sustaining the good cycle stability. The developed porous structure modifies the properties of Li intercalation/deintercalation in the composite, making a great contribution to the enhanced lithium storage performance of the ZnO-loaded/PC composite anode.

AUTHOR INFORMATION

Notes

The authors declare no competing financial interest.

ACKNOWLEDGMENTS

We acknowledge the National 973 Program (Grant No. 2009CB220100) and the National 863 Program (2013AA050903) of China for the financial support of this work. We also thank the support from U.S. - China Clean Energy Research Center Clean Vehicles Consortium (Grant No. 2010DFA72760-101).

REFERENCES

(1) Lu, L. G.; Han, X. B.; Li, J. Q.; Hua, J. F; Ouyang, M. G. *J. Power Sources* **2013**, *226*, 272−288.
(2) Chandrashekar, S.; Trease, N. M.; Chang, H. J.; Du, L. S.; Grey, C. P.; Jerschow, A. *Nat. Mater.* **2012**, *11*, 311−315.
(3) Teki, R. K.; Moni, D.; Krishnan, R.; Thomas, C. P.; Prashant, N. K.; Koratkar, N. *Small* **2009**, *5*, 2236−2242.
(4) Huang, X. H.; Wu, J. B.; Lin, Y.; Guo, R. Q. *Int. J. Electrochem. Sci.* **2012**, *7*, 6611−6621.
(5) Sun, Y. M.; Seo, J. H.; Takacs, C. J.; Seifter, J.; Alan, J. H. *Adv. Mater.* **2011**, *23*, 1679−1683.
(6) He, J. H.; Ke, J. J; Chang, P. H.; Tsai, K. T.; Yang, P. C.; Chan, I. M. *Nanoscale* **2012**, *4*, 3399−3404.
(7) Tian, S. Q.; Yang, F.; Zeng, D. W.; Xie, C. S. *J. Phys. Chem. C* **2012**, *116*, 10586−10591.
(8) Wen, R. J.; Yang, Z. H.; Fan, X. M.; Tan, Z. Y.; Yang, B. *Electrochim. Acta* **2012**, *83*, 376−382.
(9) Wu, M. S; Chang, H. W. *J. Phys. Chem. C* **2013**, *117*, 2590−2599.
(10) Wang, H.; Pan, Q. M.; Cheng, Y. X.; Zhao, J. W.; Yin, G. P. *Electrochim. Acta* **2009**, *54*, 2851−2855.
(11) Wang, J. Z.; N. Zhang, D. H.; Yu, J. X.; Yang, D. R. *Mater. Res. Bull.* **2011**, *46*, 2378−2384.
(12) Lee, J. H.; Hon, M. H.; Chung, Y. W. *Appl. Phys. A: Mater. Sci. Process.* **2011**, *102*, 545−550.
(13) Zhang, C. Q.; Tu, J. P.; Yuan, Y. F.; Huang, X. H.; Chen, X. T.; Mao, F. *J. Electrochem. Soc.* **2007**, *154*, A65−A69.
(14) Liu, J.; Li, Y. Y.; Ding, R. M.; Jiang, J.; Hu, Y. Y.; Ji, X. X.; Chi, Q. B.; Zhu, Z. H.; Huang, X. T. *J. Phys. Chem. C* **2009**, *113*, 5336−5339.
(15) Qin, L .M.; Zhu, Q.; Li, G. R.; Liu, F. T.; Pan, Q. M. *J. Mater. Chem.* **2012**, *22*, 7544−7550.
(16) Zhou, Y. N.; Li, W. J.; Fu, Z. W. *Electrochim. Acta* **2012**, *59*, 435−440.
(17) Wu, Z.; Qin, L. M.; Pan, Q. M. *J. Alloys Compd.* **2011**, *509*, 9207−9213.
(18) Yang, S. B.; Song, H. H.; Chen, X. H. *Electrochem. Commun.* **2006**, *8*, 137−141.
(19) Huang, X. H.; Xia, X. H.; Yuan, Y. F.; Zhou, F. *Electrochim. Acta* **2011**, *56*, 4960−4965.
(20) Shen, L. F; Uchaker, E.; Yuan, C. Z; Nie, P.; Zhang, M.; Zhang, X. G.; Cao, G. Z. *ACS Appl. Mater. Interfaces* **2012**, *4*, 2985−299.
(21) Yu, Z. Y.; Zhu, S. M.; Li, Y.; Liu, Q. L.; Feng, C.; Zhang, D. *Mater. Lett.* **2011**, *65*, 3072−3075.
(22) Liu, J.; Zhou, Y. C.; Liu, F.; Liu, C. P.; Wang, J. B.; Pan, Y.; Xue, D. F. *RSC Adv.* **2012**, *2*, 2262−2265.
(23) Shen, X. Y.; Mu, D. B.; Chen, S.; Xu, B.; Wu, B. R.; Wu, F. *J. Alloys Compd.* **2013**, *552*, 60−64.
(24) Zhou, H. S.; Zhu, S. M.; Hibino, M.; Honma, I.; Ichihara, M. *Adv. Mater.* **2003**, *15*, 2107−2111.
(25) Yang, Z. H.; Luan, C. Y.; Zhang, W. X.; Liu, A. P.; Tang, S. P. *Thin Solid Films* **2008**, *516*, 5974−5980.

(26) Shi, L.; Lin, H. L.; Bao, K. Y.; Cao, J.; Qian, Y. T. *Nanoscale Res. Lett.* **2009**, *5*, 20−24.
(27) Sharma, Y.; Sharma, N.; Rao, S. G. V.; Chowdari, B. V. R. *Adv. Funct. Mater.* **2007**, *17*, 2855−2861.
(28) Ahmad, M.; Shi, Y.; Nisar, A.; Sun, H.; Shen, W.; Wei, M.; Zhu, J. *J. Mater. Chem.* **2011**, *21*, 7723−7729.
(29) Han, F.; Li, D.; Li, W. C.; Lei, C.; Sun, Q.; Lu, A. H. *Adv. Funct. Mater.* **2012**, 1−9.
(30) Zhou, G.; Wang, D. W.; Yin, L. C.; Li, N.; Li, F.; Cheng, H. M. *ACS Nano* **2012**, *6*, 3214−3223.
(31) Coetzee, J. F.; Gardner, C. W. *Anal. Chem.* **1982**, *54*, 2530−2532.
(32) Liu, H.; Wang, G. X.; Liu, J.; Qiao, S. Z.; Ahn, H. *J. Mater. Chem.* **2011**, *21*, 3046−3052.
(33) Wang, G. X.; Zhong, S.; Bradhurst, D. H.; Dou, S. X.; Liu, H. K. *Solid State Ionics* **1999**, *116*, 271−277.
(34) Wang, X. Y.; Hao, H.; Liu, J. l.; Huang, T.; Yu, A. S. *Electrochim. Acta* **2011**, *56*, 4065−4069.
(35) Yuan, C. Z.; Hou, L. R.; Shen, L. F.; Li, D.; Zhang, F.; Fan, C. G.; Li, J. M.; Zhang, X. G. *Electrochim. Acta* **2010**, *56*, 115−121.
(36) Ding, R.; Qi, L.; Wang, H. W. *J. Solid State Electrochem.* **2012**, *16*, 3621−3633.